Huang, Z., Tilmann, F., Xu, M., Wang, L., Ding, Z., Mi, N., Yu, D., Li, H. (2017): Insight into NE Tibetan Plateau expansion from crustal and upper mantle anisotropy revealed by shear-wave splitting. - *Earth and Planetary Science Letters*, *478*, pp. 66—75.

DOI: http://doi.org/10.1016/j.epsl.2017.08.030

Insight into NE Tibetan Plateau expansion from crustal and upper mantle anisotropy revealed by shear-wave splitting

Zhouchuan Huang[a,b,c,*], Frederik Tilmann[c,e], Mingjie Xu[a,b], Liangshu Wang[a,b], Zhifeng Ding[d], Ning Mi[a,b], Dayong Yu[a,b], Hua Li[a,b]

a. State Key Laboratory for Mineral Deposits Research, School of Earth Sciences and Engineering, Nanjing University, Nanjing 210046, China

b. Institute of Geophysics and Geodynamics, Nanjing University, Nanjing 210046, China

c. GeoForschungsZentrum Potsdam, Telegrafenberg, Potsdam 14473, Germany

d. Institute of Geophysics, China Earthquake Administration, Beijing 100081, China

e. Freie Universität Berlin, Berlin 14195, Germany

*Corresponding author: huangz@nju.edu.cn (Z. Huang)

Abstract: The northeastern Tibetan plateau margin is the current expansion border, where growth of the plateau is ongoing. We analyse shear-wave splitting at ChinArray stations in the NE Tibetan Plateau and its margin with the stable North Chine Craton. The measurements provide important information on the seismic anisotropy and deformations patterns in the crust and upper mantle, which can be used to constrain the expansion mechanism of the plateau. Along the margin and within the craton, the dominant NW-SE fast polarization direction (FPD) is NW-SE, subparallel to the boundary between the plateau and the North China Craton. The shear-wave splitting measurements on the NE Tibetan Plateau itself generally reflect two-layer anisotropy. The lower-layer anisotropy (with NW-SE FPDs) is consistent in the whole region and FPDs are the same as those in the North China Craton. The upper-layer FPDs are parallel to the boundary orogens and faults along the NE Tibetan Plateau margin and are parallel to crustal motion rather than surface structures within the high plateau. The two-layer anisotropy implies the presence of deformed Tibetan lithosphere above the underthrusting North China Craton. The NE Tibetan shows similar deformation patterns at the surface (inferred from GPS) and within the mantle (inferred from shear-wave splitting), but significant crustal anisotropy (parallel to crustal motion) requires mid-lower crustal channel flow or detachment to drive further tectonic uplift of the plateau.

Keywords: ChinArray; Tibetan Plateau; Shear-wave splitting; Seismic anisotropy;

Underthrusting lithosphere; Crustal channel flow/detachment

1 Introduction

The Tibetan Plateau has been forming in response to the Indo-Asian collision since ~50 Ma (Fig. 1a) (e.g., Royden et al., 2008; Yin and Harrison, 2000; Zhu et al., 2015). Many different models have been proposed for its evolution, which generally include discrete intracontinental subduction coupled with lateral extrusion along major strike-slip faults (Tapponnier et al., 2001), underthrusting of Indian and Asian lithosphere beneath the Tibetan Plateau (e.g., Kind et al., 2002; Ye et al., 2015; Zhao et al., 2010, 2011), distributed shortening of the Asian crust or lithosphere (e.g., England and Houseman, 1986; Zhang et al., 2004), and lateral channel flow in the mid-lower crust (Clark and Royden, 2000; Royden et al., 1997, 2008). These models predict different deformation patterns and thus different patterns of seismic anisotropy in the crust and upper mantle (Silver, 1996).

Seismic anisotropy arises from preferred orientations of minerals or micro-structures in response to shearing (Karato et al., 2008). Dislocation creep aligns the constituent minerals such as amphibole and mica in the mid-lower crust and olivine in the upper mantle, causing lattice preferred orientation (LPO) (Ji et al., 2015; Karato et al., 2008). The fast orientation is generally parallel to the axis of maximum extension, which is aligned with the direction of maximum shear for large shear strains. It is often found to be subparallel to active strike-slip faults and orogenic fronts. For simple mantle flow in the asthenosphere, the fast orientation generally reflects the mantle flow direction due to shearing in the asthenosphere (Karato et al., 2008). In the special case of channelized plastic flow in the mid-lower crust, the relationship between the fast orientation and the flow direction depends on the differential stress level and temperature (Ko and Jung, 2015). For the high differential stresses and high temperatures under the Tibetan Plateau, the fast orientation is sub-parallel to the flow direction (Ko and Jung, 2015).

The different models introduced earlier produce different seismic anisotropy patterns in the crust and upper mantle beneath the Tibetan Plateau. Lateral extrusion along strike-slip faults would induce extensive deformation along the boundary faults, hence the anisotropy near the boundary would be expected to be much stronger than in the block interior. In contrast, the distributed shortening model suggests only slowly varying vertically coherent anisotropy in the whole region, both near the boundary and in the interior. Lithospheric underthrusting would introduce another layer of anisotropy beneath the deformed Tibetan lithosphere and thus give rise to multi-layer anisotropy. Finally, lateral channel flow in the mid-lower crust would also produce similar two-layer anisotropy, but the anisotropy would be closely related to the channelized ductile deformation rather than the lithospheric deformation caused by the India-Asian convergence.

In this study, we analyze data from the ChinArray project, which deployed hundreds of broadband stations with a lateral spacing of ~20-30 km across the NE

Tibetan Plateau from 2013 to 2016. The dense array covered the eastern Qilian Orogen and West Qinling as well as the western North China Craton surrounding the NE Tibetan Plateau (Fig. 1a). The unprecedented high-quality data makes it possible to image high-resolution structures in the crust and upper mantle in this region. The NE Tibetan Plateau is of particular interest because here it interacts with the stable Eurasian Plate (e.g., North China Craton) (Fig. 1). Lateral extrusion along large sinistral strike-slip faults such as the Altyn-Tag Fault, the Kunlun Fault, and the Haiyuan Fault probably plays an important role in shaping the crustal tectonics in the expansion frontier (e.g., Burchfiel et al., 1989; Cheng et al., 2015; Duvall et al., 2013; Yuan et al., 2013). However, extensive thrust systems, which have developed mainly in the Qilian Shan thrust belt and to a minor degree also in West Qinling and the Liupan Shan, could have accumulated more than 50% of the crustal strain in the Cenozoic (e.g., Cheng et al., 2015; Craddock et al., 2014; Gao et al., 2013; Lease et al., 2012; Yin et al., 2008; Zuza et al., 2016). The strain rates inverted from continuous GPS measurements are much higher near these faults and thrust belts than adjacent regions (Fig. 1b) (Kreemer et al., 2014).

Compared with the well documented crustal structures and tectonics, the structures and especially deformations in the upper mantle are less clear. Previous studies used shear-wave splitting method to reveal the general pattern of seismic anisotropy below the NE Tibetan Plateau (León Soto et al., 2012; Li et al., 2011; Wang et al., 2008, 2016; Wu et al., 2015; Ye et al., 2016; Zhang et al., 2012). In general, the dominant fast orientations of seismic anisotropy follow the large-scale trend of the tectonic boundary. Pms splitting (conversions from teleseismic P to S waves at the Moho) at permanent stations shows some notable variations that were interpreted as evidence for mid-lower crustal flow (e.g., Kong et al., 2016; Shen et al., 2015). These studies were based on sparse station sets, so they cannot provide details of the lateral variations especially in different blocks and their boundaries. Chang et al. (2017) measured shear-wave splitting with the data recorded by the ChinArray project in NE Tibetan Plateau. However, they assumed single-layer anisotropy and did not consider potential multi-layer anisotropy. In this study, we analyzed teleseismic shear-wave splitting and obtained reliable splitting parameters to study seismic anisotropy in the crust and upper mantle in the NE Tibetan Plateau. We measured and compared the shear-wave splitting in different tectonic units, especially contrasting the measurements close to the tectonic boundaries or faults from those farther away. Furthermore, we carefully analyzed the measurements for backazimuthal variations to reveal two-layer anisotropy, which indicates depth-dependency of the deformation pattern. These observations provide new information on the crustal and upper mantle deformation patterns and thus help us to better understand the tectonic models of the Tibetan Plateau evolution.

2 Data and Methods

2.1 Data

The waveforms were recorded by 173 temporary broadband stations (Fig. 2a) deployed by the ChinArray project from October 2013 to March 2015. Each station was equipped with a Guralp CMG-3EPC three-component broadband seismometer and a Reftek-130 digitizer, all sampling at 100 Hz. We selected events with magnitudes greater than 5.5 and epicentral distances of 85°-150º. We visually inspected the core phases SKS, SKKS, and PKS phases and selected clear arrivals in the waveforms of 92 events (Fig. 2b) for further analysis. Most of the events are located near the Tonga and New Zealand subduction zones and in North America. Some mid-oceanic ridge events in the Atlantic and Indian oceans increase the back-azimuthal coverage.

2.2 Methods

Shear-wave splitting analysis describes the phenomenon that a shear-wave splits into two perpendicular waves travelling with different speeds. By analyzing the horizontal components of one single event recorded at a station, we can obtain the splitting parameters, fast polarization direction (FPD), φ, and delay time difference between the fast and slow waves, δt, that represent the fast orientation of anisotropy and the strength of anisotropy or thickness of the anisotropic layer, respectively (Silver and Chan, 1991). Phases converted from P to S at the core-mantle boundary are the most popular phase to analyze for splitting because the core acts as a polarization filter, ensuring the waves are polarized in radial direction prior to encountering any anisotropic structure below the target region.

We used the minimum transverse energy method as implemented by the SplitLab toolbox to measure shear-wave splitting parameters (Figs. S1-S5) (Silver and Chan, 1991; Wüstefeld et al., 2008). The method finds the optimal splitting parameter by minimizing the signal on the corrected transverse component with a grid search algorithm in a ray-coordinate based L–Q–T coordinate system. The search ranges for φ and δt are 0-180º with a step of 1º and 0-3.0 s with a step of 0.02 s, respectively. The uncertainties are estimated by the 95% confidence region of the F-test (Figs. S1f and S1i) with the updated calculation of the degrees of freedom (Walsh et al., 2013).

We improved the process by selecting the time window automatically as well as changing the window lengths iteratively to find the splitting parameters with minimal uncertainties (i.e., 95% confidence region). We determined the beginning of the time window referring to the STA/LTA ratio (short-time to long-time average ratio) on the radial component around the theoretical arrival time of the used phase (from -10 to 10 s) (Fig. S1b). The length of the time window changes incrementally from 1 to 2.5 times the dominant period; the window length step corresponds to 1/10 of the dominant period (Fig. S1b). The iteration terminates earlier if the ending otherwise falls into the window of the direct S wave. We applied an additional criterion to accelerate the process by comparing the average energy in the corrected transverse component for the N-th iteration (e.g., E_N) with that for the previous (N-1-th) iteration (i.e., $E_{N\text{-}1}$). If $\frac{E_N}{E_{N\text{-}1}} > 1.2$, we consider that additional factors other than splitting influent the analysis so that we terminate the iteration. We plot original and corrected particle motions (Figs. S1d and S1g) and radial and transverse components (Figs. S1e and S1h), the map of energy on the transverse component (Figs. S1f and S1i), as well as the splitting parameters of all iterations (Fig. S1c). We visually checked all the analysis results and classified them — mostly based on the linearity of the corrected particle motion and the consistency of the measurements for different time windows — into 'good', 'fair', 'poor' and 'null' measurements. Normally, the solution with the smallest estimated uncertainty ('optimal' solution) is taken as the final result, but sometimes this solution is deemed less stable, because it corresponds to a very short analysis window; in this case the measurement corresponding to the maximum length time window was chosen as the preferred one. In nearly all 'good' and 'fair' measurements, the differences are very small anyway. The semi-automatic shear-wave splitting analysis accelerates the measurements, which makes it possible to measure shear-wave splitting in different frequency bands (discussed later) for the large number of stations in NE Tibet. At the same time, it estimates the possible influence of different time windows on the results and this helps to improve the reliability of the results.

We search for potential models of two-layer anisotropy with a grid-search algorithm (Silver and Savage, 1994), where the parameters are the fast directions of the upper and lower layer, Φ_{U} and Φ_{L}, and corresponding delay times ΔT_U and ΔT_L. The method searches for the optimal model that minimizes the misfit (r) between the synthetic and observational parameters, which is defined as:

$$r = \sum_{i=1}^{N} \left[\left(\frac{\varphi_i^{obs} - \varphi_i^{syn}}{\sigma_i^{\varphi}} \right)^2 + \left(\frac{\delta t_i^{obs} - \delta t_i^{syn}}{\sigma_i^{\delta t}} \right)^2 \right]$$

where $(\varphi_i^{obs}, \delta t_i^{obs})$ and $(\varphi_i^{syn}, \delta t_i^{syn})$ are the $\boldsymbol{i}$-th $(i = 1 \dots N)$ observational and synthetic parameters, respectively, σ_i^{φ} and $\sigma_i^{\delta t}$ are the corresponding 95% uncertainties. The search ranges for $\Phi_{\mathrm{U,L}}$ and $\Delta T_{U,L}$ are 0º-180º with a step of 2º and 0-1.5 s with a step of 0.05 s, respectively, for two-layer anisotropy. A fitting parameter R^* is used to estimate the degree to which two-layer models fit the observations better than a single-layer model with horizontal fast axis (Fontaine et al., 2007):

$$R^* = 1 - \frac{(N_d\text{-}1)}{N_d\text{-}k\text{-}1} \times (1 - \mathrm{R}^2)$$

where N_d is the number of observations (i.e., 2N), and $\mathrm{k}(= 4)$ is the number of model parameters, R^2 $(= 1 - r_2/r_1)$ is the reduction of the misfits between observational and synthetic splitting parameters for the two-layer models (r_2) compared with the optimal one-layer model (r_1). We take models with $R^* \geq 0.20$ as valid two-layer models as they explain more than 20% of the variations in observations (Fontaine et al., 2007; Walker et al., 2005). However, no accurate uncertainties are calculated in the method.

3 Results

3.1 Shear-wave splitting measurements

We measured shear-wave splitting in two different frequency or period bands, i.e., low-frequency (LF) at 8-20 s and high-frequency (HF) at 2-8 s. From the viewpoint of finite-frequency seismology, the seismogram recorded by a station is influenced by the structure within a certain distance around the ray path. The approximate radius of the sensitivity range (i.e., 1st Fresnel zone) is ~100 km and ~50 km in the uppermost mantle for typical SKS phases with a dominant period of 8 s and 4 s, respectively (Favier and Chevrot, 2003; Rümpker and Ryberg, 2000). Thus results measured at 8-20 s are actually regional average measurements while those measured at 2-8 s could better reveal high-resolution lateral variations of anisotropy. Furthermore, the high-frequency seismograms tend to capture more structures in the shallow part (Favier and Chevrot, 2003) and so could be more sensitive to crustal anisotropy.

We obtained 368 “good”, 482 “fair”, 753 “poor”, and 857 “null” measurements for LF waveforms (8-20 s) and 218 “good”, 609 “fair”, 248 “poor”, and 90 “null” measurements for HF waveforms (2-8 s). The dominant periods of the waveforms for LF and HF measurements are in the ranges of 9-14 s and 4-7 s, respectively (Fig. 3a); the corresponding radii of the 1st Fresnel zone of the shear-wave splitting measurements are 100-200 km and 50-100 km, respectively, in the crust and upper mantle. Dominant FPDs for both LF and HF measurements are NW-SE (Group I) (Fig. 3d), which is consistent with the “null” measurements (Fig. 3b). However, a number of measurements show ENE-WSW to nearly E-W FPDs (Group II) (Fig. 3d), especially for the HF measurements. The FPDs deviate by ~20° from the absolute plate motion (APM) direction in the NE Tibetan Plateau (Fig. 3d). Delay times (δt) of the HF measurements (i.e., dominantly 0.4-1.5 s) are generally smaller than those of the LF measurements (0.8-2.5 s) (Fig. 3c). We note that the uncertainties of the LF measurements are usually larger, which may cause more scattered measurements and some large δt values.

The overall FPDs in the NE margin of the Tibetan Plateau are mostly parallel to the strikes of the major tectonic boundaries (Figs. 4 and 5): they generally follow the NW strikes of the Qilian Orogen and Haiyuan Fault in the north and slightly rotate to be parallel to the NNW strike of the Liupan Shan in the east. These measurements are generally consistent with first-order patterns in previous results (Chang et al., 2017; León Soto et al., 2012; Li et al., 2011; Wang et al., 2016; Ye et al., 2016; Zhang et al., 2012) and continue in Gobi-Altay and Central Mongolia (Fig. 1a) ~1000 km north of NE Tibetan Plateau (Barruol et al., 2008; Qiang et al., 2017). The large-scale pattern of FPDs is parallel to anisotropy in the crust and upper mantle revealed by P-wave anisotropic tomography (Huang et al., 2014) and surface wave tomography (Pandey et al., 2015) in the NE Tibetan Plateau.

In contrast, NE-SW and nearly E-W FPDs are observed beneath West Qinling at elevations above 3000 m (Figs. 4 and 5). Similar FPDs were also obtained in previous studies (e.g., Li et al., 2011; Wu et al., 2015; Ye et al., 2016), even near 94°E that is ~800 km westward from West Qinling (León Soto et al., 2012). The orientations deviate from the strikes of surface geology (e.g., faults) significantly. Therefore, the origin of anisotropy in West Qinling is probably different from that in the NE frontier (i.e., along the Qilian Orogen, Haiyuan Fault, and Liupan Shan).

3.2 Two-layer anisotropy

In addition to the lateral variations as described above, the shear-wave splitting measurements at many stations show notable azimuthal variations. Previous studies argued that the azimuthal variations can be explained by a two-layer anisotropy model under West Qinling (Li et al., 2011; Ye et al., 2016). Here, we fit the shear-wave splitting measurements with two-layer models in moving spatial windows (fixed to grid nodes), as there is an insufficient number of measurements at individual stations. Grid nodes are placed 0.5° intervals of latitude and longitude. All measurements whose raypaths at 0-200 km depth are completely contained within a cylinder of 50 km radius around the grid node are taken into account for the estimate of the two-layer splitting parameters.

We applied the method to both the LF and HF measurements, and confirm the presence of two-layer anisotropy model for ten grid nodes for the HF measurements (Figs. 6 and S6), nine of which are located in West Qinling and the Qilian Orogen. FPDs of upper and lower layers are fairly well constrained for reliable models ($R^* \geq 0.20$) even though the delay times appear to scatter quite a bit (Fig. S6). The FPDs in the lower layer align NW-SE and are generally consistent with the regional pattern of measurements in the NE margin of the plateau. The fast orientations in the upper layer align between ENE-WSW and E-W, which is subparallel to surface velocities determined from GPS observations (Gan et al., 2007). Delay times of the upper and lower layers are in the ranges of 0.5-0.8 s and 1.0-1.5 s, respectively. These two-layer splitting parameters are consistent with those obtained by Li et al. (2011) in the NE Tibetan Plateau. The grid node close to Haiyuan Fault (grid node a in Fig. 6) is a special case, where the upper layer FPD is close to the fault and ΔT_U is especially large (~1.5 s). A similar measurement is obtained for a grid node (marked b in Fig. 6) in West Qinling. We suspect that these anomalous ΔT_U values are caused by a numerical instability as the statistics do not imply local peaks around these values (Fig. S6). The observations near the Liupan Shan also require two-layer anisotropy. The lower-layer FPD follows the regional average (i.e., NW-SE) while the upper-layer FPD (NNW-SSE) is approximately parallel to the strike of the Liupan Shan.

We compare our results to Pms splitting measurements at permanent stations in the study area (Kong et al., 2016; Shen et al., 2015; Wang et al., 2016). With the exception of a station near the Maxianshan Fault, where the Pms fast direction parallels to our estimate of the upper-layer anisotropy, Pms fast directions are generally not parallel to our upper layer results but instead align with the strikes of nearby faults (Fig. 7). The discrepancy may result from the different frequency bands used in the Pms measurements (~1.0 s) and our HF waveforms (2-8 s). Pms splitting is more sensitive to anisotropy in the upper crust (Favier and Chevrot, 2003). Most of the Pms splitting measurements are close to active faults; where complex crustal structures related to the fault activities may produce stronger anisotropy and affect the observations (e.g., León Soto et al., 2012).

We could not obtain a reliable two-layer model for any grid node for the LF measurements because of two effects. First, the uncertainties of the LF measurements are usually so large that the azimuthal variations of the splitting parameters are not compelling. Second, the LF waveforms have long wavelengths and so are less sensitive to small-scale structures, either horizontally or vertically.

4 Discussion

4.1 Seismic anisotropy beneath North China Craton

The pattern of shear-wave splitting measurements in the North China Craton is simple, with few lateral variations. The NW-SE FPDs continue northward to the Gobi-Altay and even into Central Mongolia ~1000 km north of NE Tibetan Plateau (Barruol et al., 2008; Qiang et al., 2017). Therefore there should be a generally applicable mechanism for seismic anisotropy in this broad region from the North China Craton to Central Mongolia. Three mechanisms could explain the shear-wave splitting observations: 1) “fossil” lithospheric anisotropy imprinted during the formation of the Central Asian Orogenic Belt since the Paleozoic; 2) anisotropy in the lithosphere due to present-day deformation; 3) anisotropy due to shearing in the asthenosphere driven by plate motion (Barruol et al., 2008).

The Central Asian Orogenic Belt was formed by the accretions of micro-continents and island arcs around the Siberian craton from late Cambrian to the

Triassic (e.g., Delvaux et a., 1995; Windley et al., 2007). The Sayan-Baikal fold belt was formed in western and central Mongolia accompanying the closure of the Paleo-Asian Ocean in the Caledonian, which produced NW-SE trending crustal foliations and fault-related structures. The structures were strengthened by another NW-SE trending subduction (along the present Gobi-Altay range) during Devonian to Carboniferous. Located at the southern margin of the Central Asian Orogenic Belt, the lithosphere beneath the western North China Craton and the Gobi-Altay could still preserve the deformation history in the form of anisotropy frozen into the lithosphere (Barruol et al., 2008). Afterwards, the Central Asian Orogenic Belt was re-activated in the Cenozoic due to the India-Asian collision (Delvaux et a., 1995; Windley et al., 2007). The present-day deformation may also produce significant anisotropy, which could be superimposed on the "fossil" anisotropy. However, the strain rates in the North China Craton and Gobi-Altay are mostly smaller than $10\times10^{-9}/yr$, which are only ~10% of those in the NE Tibetan Plateau (Fig. 1b) (Chang et al., 2017; Kreemer et al., 2014). Nevertheless, the shear-wave splitting delay times are similar in both these regions. Hence, the present-day deformations are unlikely to be the dominant mechanism for producing the lithospheric anisotropy.

The average thickness of the lithosphere in the western North China Craton and Central Mongolia is mostly smaller than 100 km (An and Shi, 2006; Pasyanos et al., 2014), which may account for shear-wave splitting of ~0.9 s assuming a typical anisotropy strength of 4% in the upper mantle (Silver and Chan, 1991). This value is comparable to the HF splitting delay measurements but smaller than the LF measurements. Many delay times are 1.5-2.0 s in Central Mongolia (Barruol et al., 2008; Qiang et al., 2017). Thus significant anisotropy in the asthenosphere is necessary to account for the shear-wave splitting in the North China Craton and Central Mongolia. The average difference between the shear-wave splitting FPDs and APM directions in this area is ~20°, but the asthenospheric flow is likely to be deflected around the deep roots of the stable Siberian craton and turns to be parallel to the FPDs (Barruol et al., 2008). Moreover, as discussed later, the Eurasian lithosphere is underthrusting beneath the NE Tibetan Plateau (Ye et al., 2016; Zuza et al., 2016), which could further modify the flow and cause deviation from the APM direction.

A clearer indication of the asthenospheric anisotropy is the two-layer anisotropy model found in station ULN in eastern Mongolia (Fig. 1a) (Barruol et al., 2008), which belongs to the eastern segment of the Central Asian Orogenic Belt. Here, a NE-SW trending orogen formed as a result of the closure of the Mongol-Okhotsk ocean during the Devonian to Triassic (Delvaux et a., 1995; Windley et al., 2007). The NE-SW FPD of the upper-layer anisotropy is parallel to this local orogenic strike and thus reflects the fabric of the lithosphere. Instead, the NW-SE FPD of the lower-layer anisotropy is the same as the FPDs observed in Central Mongolia, which are better explained by the asthenospheric anisotropy (Barruol et al., 2008).

4.2 Seismic anisotropy in the deformed NE Tibetan Plateau margin

The shear-wave splitting measurements in the NE Tibetan Plateau and the North

China Craton show broadly similar FPDs and splitting delay times. Although the FPDs rotate from WNW-ESE in the Qilian Orogen to NNW-SSE in the Liupan Shan (Figs. 4 and 5), these rotations most likely are caused by variation of the shallow anisotropic structure (whose FPDs tends to align parallel to orogens and faults), whereas the deeper anisotropic layer is associated with nearly uniform NW-SE FPDs (Fig. 6). The thrust faults developed in the eastern Qilian Shan and Liupan Shan could produce significant anisotropy in the crust (e.g., Burchfiel, 1989, 1991; Zhang et al., 1991; Zheng et al., 2006) sufficient to explain the upper-layer splitting delays.

A straightforward explanation for these observations is that the North China Craton is underthrusting the NE Tibetan Plateau, so that the NW-SE trending anisotropy in the North China Craton continues to be recorded even under the plateau. S wave receiver functions imaged an inclined lithosphere-asthenosphere-boundary (LAB) that deepens from 120 km below the North China Craton to 150 km below the West Qinling (Ye et al., 2015). The image of a ~30 km offset between the Eurasian LAB and the Tibetan LAB (~120 km) under the West Qinling Fault supports the notion of Eurasian lithosphere (i.e., the North China Craton) having underthrust the NE Tibetan Plateau for a considerable distance (Ye et al., 2015; Zuza et al., 2016).

Our observations of two-layer splitting in West Qinling imply significant anisotropy in the Tibetan mantle lithosphere and underlying asthenosphere (Fig. 6). As discussed later, the upper layer is probably located in the mid-lower crust. The NW-SE FPDs for the lower-layer anisotropy are similar to the measurements in the

North China Craton. However, the underthrusting Eurasian lithosphere terminates under the West Qinling Fault and does not continue southward in S wave receiver function images (Ye et al., 2015). Hence the lower-layer NW-SE FPDs in West Qinling result from anisotropy in the Tibetan mantle lithosphere and asthenosphere. The good correlation between the continuous surface deformation field (inferred from GPS observations and fault slip data) and shear-wave splitting FPDs appears to suggest that the anisotropy in NE Tibetan Plateau is produced by vertically coherent deformation in the lithosphere (e.g., Chang et al., 2017). However, the weak mid-lower crust cannot transport the stresses in the upper crust into the upper mantle or vice versa. Instead, similar surface and upper-mantle deformation patterns can be maintained by applying the same boundary forces laterally. Distributed lithospheric deformation could thus produce the same NW-SE trending anisotropy (e.g., Chang et al., 2017; England and Houseman, 1986; Zhang et al., 2004) in the upper crust and mantle lithosphere (Huang et al., 2014; Pandey et al., 2015) in spite of a weak mid-lower crustal layer in between.

Deformation in the mantle lithosphere cannot explain the whole splitting delay. The thickness of the NE Tibetan mantle lithosphere is only ~60 km (subtracting ~60 km crust from ~120 km total lithosphere), which could produce splitting delay times of ~0.5 s, only about half of the observed lower-layer delay times (1.0-1.5 s; Fig. 6). Another possible cause for anisotropy is in the asthenospheric flow driven by APM or induced by the advancing front of the underthrusting lithosphere. The average misfit between APM and lower layer FPD is ~10° (Fig. 6), which generally lies within in the confidence regions of shear-wave splitting measurements and APM directions. Meanwhile, the APM-driven asthenospheric flow may be modified by the geometry of the underthrusting Eurasian lithosphere, in particular the ~30 km step between the NE Tibetan and Eurasian LAB (Ye et al., 2015) would direct the flow along the front of the underthrusting cratonic lithosphere, i.e., in general, being parallel to the tectonic boundaries visible at the surface.

4.3 Mid-lower crustal channel flow or detachment

The upper-layer anisotropy obtained in West Qinling (in places with elevations of more than 3000 m) (Fig. 6) requires other mechanisms, as the observed FPDs (between ENE-WSW and E-W) differ significantly (>20°) from those predicted by coherent lithospheric deformation (Chang et al., 2017) and also deviate from the strikes of the major faults and orogenic fronts. Instead, the FPDs (i.e., between ENE-WSW and E-W) are sub-parallel to the crustal motion determined from GPS observations (Fig. 6). Surface wave tomography revealed low S-velocities with positive radial anisotropy (i.e., $V_{SH}>V_{SV}$) in the mid-lower crust (Figs. 7 and 8) (Bao et al., 2013; Xie et al., 2017). P wave anisotropic tomography also found anisotropic layers with NE-SW to ENE-WSW fast velocity directions at 40 and 65 km depths (Huang et al., 2014), which is equivalent to the upper-layer anisotropic layer found in this study (Fig. 8c).

Mid-lower crustal channel flow originating from the central and southern Tibetan

Plateau (e.g., Clark and Royden, 2000; Royden et al., 1997, 2008) provides a plausible explanation for these observations. Shear-wave anisotropy in the mid-lower crust can be induced by LPO of mica and amphibole developed in the channel flow (Ji et al., 2015; Ko and Jung, 2015; Shapiro et al., 2004). Mineral experiments show that the difference between the fast and slow S-wave velocity in mica- and amphibole-bearing metamorphic rocks may be as high as 0.377 km/s for samples from East Tibet (Ji et al., 2015). This difference is equivalent to an S-wave anisotropy of >10% assuming an average S-wave velocity of 3.5 km/s in the anisotropic layer (Fig. 7). Then a crustal layer of 20-30 km (Fig. 8) is easily sufficient to produce the inferred upper-layer splitting delay of 0.5-0.8 s in this study.

The structures in and around the Longzhong Basin are of particular interest. The crust may be extruding southeastward along the Haiyuan and Qinling faults above a ductile shear zone in the middle crust (Cheng et al., 2015; Gan et al., 2007; Guo et al., 2016). Significant uplift occurs around the edges of the basin with uplift rates of 2-4 mm/yr while much lower uplift rates or even subsidence are found in the interior of the Longzhong Basin (Liang et al., 2013) (Fig. 6). Low velocity bodies in the mid-lower crust beneath the West Qinling spread across West Qinling Fault in a narrow finger and reach approximately the Maxianshan Fault in the SW Longzhong Basin (Fig. 7) (Bao et al., 2013). These lower velocities correlate with significant uplift and a local high in the topography (> 2000 m). The uplift rates (~4 mm/yr) are much higher than the rates (~2 mm/yr) in West Qinling (Fig. 6) (Liang et al., 2013), which indicates that the crustal flow is blocked and thickened when it meets a strong crust. These observations support mid-lower crustal flow as a mechanism that protrudes into the stable Longzhong Basin and expands the high plateau.

An alternative process for generating mid-lower crustal anisotropy (i.e., crustal motion parallel FPDs with positive radial anisotropy) is displacement along a mid-lower crustal detachment (Klemperer, 2006). In this scenario, the upper crust moves relative to the upper mantle and drives simple shear on a weak mid-lower crust. Shortening along the Laji-Jishi and West Qinling thrust faults may account for the Cenozoic crustal thickening in the NE Tibetan Plateau (Lease et al., 2012), as found in the Qilian Shan thrust belt (e.g., Gao et al., 2013; Zuza et al., 2016). Motion along the thrust faults can induce strong uplift in West Qinling (hanging wall) and subsidence in the Longzhong Basin (footwall), which cannot be explained exclusively by the channel flow model.

Based on our results, we cannot finally conclude whether mid-lower crustal channel flow or detachments is more important because they result in almost the same seismological observations. In both cases, a 20-30 km thick anisotropic mid-lower crust is necessary to explain the shear-wave splitting observations. Klemperer (2006) showed that a combination the simple channel flow and the mid-lower crustal detachment better explains the geophysical observations in northern Tibetan Plateau. As a driving force, gravitational loading can produce horizontal extension and induce channel flow in the mid-lower crust, given the weak mid-lower crust and the topographic gradient in West Qinling (Figs. 7 and 8) (Shapiro et al., 2004). Therefore, we suggest both processes operate in the NE Tibetan Plateau (margin) and affect its evolution.

5 Conclusions

The overall pattern of shear-wave splitting anisotropy in the NE Tibetan Plateau is dominated by NW-SE oriented FPDs, which are subparallel to its tectonic boundaries with the North China Craton. In contrast to strong lateral variations of the crustal strain rates, there are no notable differences in shear-wave splitting (especially delay times) near the faults and thrust belts compared with the adjacent less deformed blocks. This pattern contradicts the prediction of the intracontinental subduction and lateral extrusion hypothesis (Tapponnier et al., 2001). Instead, the relative uniformity of the splitting measurements is consistent with distributed shortening in the lithosphere, or —alternatively or in addition — anisotropy could have developed in the asthenosphere. In west Qinling, the NE-SW FPDs measured where elevations exceed 3000 m deviate markedly from the surface texture and orientation of known faults. Two-layer anisotropic models there hint at mid-lower crustal flow or detachment as possible mechanisms for outward expansion of the plateau.

We summarize our conceptual model of the 3-D structure and deformation of the crust and upper mantle below the NE Tibetan Plateau and its margin in Fig. 9. Overall, the NE Tibetan Plateau consists of deformed lithosphere above the underthrusting

Eurasian lithosphere (i.e., North China Craton). The initial uplift of the plateau is caused by extensive thrust systems in the Qilian Shan and Liupan Shan and is accompanied by sinistral shear deformation along the Haiyuan Fault. We emphasize that the weak mid-lower crust found under the plateau is important for its further evolution. For the model with a mid-lower crustal channel below the Tibetan Plateau, the crustal flow would eventually intrude beneath the margin and cause further uplift there. For the model where the upper crust is detached and moves freely with respect to the upper mantle, strong shear is induced in the mid-lower crust. Both mechanisms require a thick mid-lower crust (20-30 km) to account for the obtained azimuthal anisotropy (parallel to crustal motion from GPS observations) and the positive radial anisotropy (V_{SH}>V_{SV}). Significant asthenospheric flow in front of the underthrusting North China Craton is indicated by our observations of strong splitting in a lower layer.

Acknowledgements. The waveform data were provided by the China Seismic Array Data Management Center at the Institute of Geophysics, China Earthquake Administration. We thank Dr. Pan Wang and Shengsi Sun for helpful discussion. Comments from Prof. An Yin (editor) and two anonymous reviewers greatly improved the manuscript. This work was supported by ChinArray Program (201308011, DQJB16A0306) and National Natural Science Foundations of China (41674044). ZH is also supported by Deng Feng Scholar Program of Nanjing

University and the Alexander von Humboldt foundation. Most figures were made using GMT (Wessel et al., 2013).

References:

An, M., Shi, Y., 2006. Lithospheric thickness of the Chinese continent. Phys. Earth Planet. Inter. 159, 257–266.

Bao, X., Song, X., Xu, M., Wang, L., Sun, X., Mi, N., Yu, D., Li, H., 2013. Crust and upper mantle structure of the North China Craton and the NE Tibetan Plateau and its tectonic implications. Earth Planet. Sci. Lett. 369–370, 129–137.

Barruol, G., Deschamps, A., Déverchère, J., Mordvinova, V.V., Ulziibat, M., Perrot, J., Artemiev, A.A., Dugarmaa, T., Bokelmann, G.H.R., 2008. Upper mantle flow beneath and around the Hangay dome, Central Mongolia. Earth Planet. Sci. Lett. 274, 221–233.

Bird, P., 2003. An updated digital model of plate boundaries. Geochem. Geophys. Geosystems 4, 1027.

Burchfiel, B.C., Quidong, D., Molnar, P., Royden, L., Yipeng, W., Peizhen, Z., Weiqi, Z., 1989. Intracrustal detachment within zones of continental deformation. Geology 17, 748–752.

Burchfiel, B.C., Zhang, P., Wang, Y., Zhang, W., Song, F., Deng, Q., Molnar, P., Royden, L., 1991. Geology of the Haiyuan Fault Zone, Ningxia-Hui Autonomous Region, China, and its relation to the evolution of the Northeastern Margin of the Tibetan Plateau. Tectonics 10, 1091–1110.

Chang, L., Ding, Z., Wang, C., Flesch, L.M., 2017. Vertical coherence of deformation in lithosphere in the NE margin of the Tibetan plateau using GPS and shear-wave splitting data. Tectonophysics 699, 93–101.

Cheng, F., Jolivet, M., Dupont-Nivet, G., Wang, L., Yu, X., Guo, Z., 2015. Lateral extrusion along the Altyn Tagh Fault, Qilian Shan (NE Tibet): insight from a 3D crustal budget. Terra Nova 27, 416–425.

Clark, M.K., Royden, L.H., 2000. Topographic ooze: Building the eastern margin of Tibet by lower crustal flow. Geology 28, 703–706.

Craddock, W.H., Kirby, E., Zhang, H., Clark, M.K., Champagnac, J.-D., Yuan, D., 2014. Rates and style of Cenozoic deformation around the Gonghe Basin, northeastern Tibetan Plateau. Geosphere 10, 1255–1282.

Deng, Q., Zhang, P., Ran, Y., Yang, X., Min, W., Chu, Q., 2003. Basic characteristics of active tectonics of China. Sci. China Ser. Earth Sci. 46, 356–372.

Delvaux, D., Moeys, R., Stapel, G., Melnikov, A., Ermikov, V., 1995. Palaeostress reconstructions and geodynamics of the Baikal region, Central Asia, Part I. Palaeozoic and Mesozoic pre-rift evolution. Tectonophysics 252, 61–101.

Duvall, A.R., Clark, M.K., Kirby, E., Farley, K.A., Craddock, W.H., Li, C., Yuan, D.-Y., 2013. Low-temperature thermochronometry along the Kunlun and Haiyuan Faults, NE Tibetan Plateau: Evidence for kinematic change during late-stage orogenesis. Tectonics 32, 1190–1211.

England, P., Houseman, G., 1986. Finite strain calculations of continental deformation: 2. Comparison with the India-Asia Collision Zone. J. Geophys. Res. Solid Earth 91, 3664–3676.

Favier, N., Chevrot, S., 2003. Sensitivity kernels for shear wave splitting in transverse isotropic media. Geophys. J. Int. 153, 213–228.

Fontaine, F.R., Barruol, G., Tommasi, A., Bokelmann, G.H.R., 2007. Upper-mantle flow beneath French Polynesia from shear wave splitting. Geophys. J. Int. 170, 1262–1288.

Gan, W., Zhang, P., Shen, Z.-K., Niu, Z., Wang, M., Wan, Y., Zhou, D., Cheng, J., 2007. Present-day crustal motion within the Tibetan Plateau inferred from GPS measurements. J. Geophys. Res. Solid Earth 112, B08416.

Gao, R., Wang, H., Yin, A., Kuang, Z., Zuza, A.V., Li, W., Xiong, X., 2013. Tectonic development of the northeastern Tibetan Plateau as constrained by high-resolution deep seismic-reflection data. Lithosphere L293.1.

Gripp, A.E., Gordon, R.G., 2002. Young tracks of hotspots and current plate velocities. Geophys. J. Int. 150, 321–361.

Guo, X., Gao, R., Li, S., Xu, X., Huang, X., Wang, H., Li, W., Zhao, S., Li, X., 2016. Lithospheric architecture and deformation of NE Tibet: New insights on the interplay of regional tectonic processes. Earth Planet. Sci. Lett. 449, 89–95.

Huang, Z., Wang, P., Zhao, D., Wang, L., Xu, M., 2014. Three-dimensional P wave azimuthal anisotropy in the lithosphere beneath China. J. Geophys. Res. Solid Earth 119, 2014JB010963.

Ji, S., Shao, T., Michibayashi, K., Oya, S., Satsukawa, T., Wang, Q., Zhao, W., Salisbury, M.H., 2015. Magnitude and symmetry of seismic anisotropy in mica- and amphibole-bearing metamorphic rocks and implications for tectonic interpretation of seismic data from the southeast Tibetan Plateau. J. Geophys. Res. Solid Earth 120, 2015JB012209.

Karato, S., Jung, H., Katayama, I., Skemer, P., 2008. Geodynamic Significance of Seismic Anisotropy of the Upper Mantle: New Insights from Laboratory Studies. Annu. Rev. Earth Planet. Sci. 36, 59–95.

Kind, R., Yuan, X., Saul, J., Nelson, D., Sobolev, S.V., Mechie, J., Zhao, W., Kosarev, G., Ni, J., Achauer, U., Jiang, M., 2002. Seismic Images of Crust and Upper Mantle Beneath Tibet: Evidence for Eurasian Plate Subduction. Science 298, 1219–1221.

Klemperer, S.L., 2006. Crustal flow in Tibet: geophysical evidence for the physical state of Tibetan lithosphere, and inferred patterns of active flow. Geol. Soc. Lond. Spec. Publ. 268, 39–70.

Ko, B., Jung, H., 2015. Crystal preferred orientation of an amphibole experimentally

deformed by simple shear. Nat. Commun. 6, 6586.
Kong, F., Wu, J., Liu, K.H., Gao, S.S., 2016. Crustal anisotropy and ductile flow beneath the eastern Tibetan Plateau and adjacent areas. Earth Planet. Sci. Lett. 442, 72–79.
Kreemer, C., Blewitt, G., Klein, E.C., 2014. A geodetic plate motion and Global Strain Rate Model. Geochem. Geophys. Geosyst. 15, 3849–3889.
Lease, R.O., Burbank, D.W., Zhang, H., Liu, J., Yuan, D., 2012. Cenozoic shortening budget for the northeastern edge of the Tibetan Plateau: Is lower crustal flow necessary? Tectonics 31, TC3011.
León Soto, G., Sandvol, E., Ni, J.F., Flesch, L., Hearn, T.M., Tilmann, F., Chen, J., Brown, L.D., 2012. Significant and vertically coherent seismic anisotropy beneath eastern Tibet. J. Geophys. Res. Solid Earth 117, B05308.
Li, Y., Wu, Q., Zhang, F., Feng, Q., Zhang, R., 2011. Seismic anisotropy of the Northeastern Tibetan Plateau from shear wave splitting analysis. Earth Planet. Sci. Lett. 304, 147–157.
Liang, S., Gan, W., Shen, C., Xiao, G., Liu, J., Chen, W., Ding, X., Zhou, D., 2013. Three-dimensional velocity field of present-day crustal motion of the Tibetan Plateau derived from GPS measurements. J. Geophys. Res. Solid Earth 118, 2013JB010503.
Pandey, S., Yuan, X., Debayle, E., Tilmann, F., Priestley, K., Li, X., 2015. Depth-variant azimuthal anisotropy in Tibet revealed by surface wave tomography. Geophys. Res. Lett. 42, 2015GL063921.
Pasyanos, M.E., Masters, T.G., Laske, G., Ma, Z., 2014. LITHO1.0: An updated crust and lithospheric model of the Earth. J. Geophys. Res. Solid Earth 119, 2013JB010626.
Qiang, Z., Wu, Q., Li, Y., Gao, M., Demberel, S., Ulzibat, M., Sukhbaatar, U., Flesch, L.M., 2017. Complicated seismic anisotropy beneath south-central Mongolia and its geodynamic implications. Earth and Planetary Science Letters 465, 126–133.
Royden, L.H., Burchfiel, B.C., Hilst, R.D. van der, 2008. The Geological Evolution of the Tibetan Plateau. Science 321, 1054–1058.
Royden, L.H., Burchfiel, B.C., King, R.W., Wang, E., Chen, Z., Shen, F., Liu, Y., 1997. Surface Deformation and Lower Crustal Flow in Eastern Tibet. Science 276, 788–790.
Rümpker, G., Ryberg, T., 2000. New “Fresnel-Zone” estimates for shear-wave splitting observations from finite-difference modeling. Geophys. Res. Lett. 27, 2005–2008.
Shapiro, N.M., Ritzwoller, M.H., Molnar, P., Levin, V., 2004. Thinning and Flow of Tibetan Crust Constrained by Seismic Anisotropy. Science 305, 233–236.
Shen, X., Yuan, X., Ren, J., 2015. Anisotropic low-velocity lower crust beneath the northeastern margin of Tibetan Plateau: Evidence for crustal channel flow. Geochem. Geophys. Geosystems 16, 4223–4236.
Silver, P.G., 1996. Seismic anisotropy beneath the continents: probing the depths of

geology. Annu. Rev. Earth Planet. Sci. 24, 385–432.
Silver, P.G., Chan, W.W., 1991. Shear wave splitting and subcontinental mantle deformation. J. Geophys. Res. Solid Earth 96, 16429–16454.
Silver, P.G., Savage, M.K., 1994. The Interpretation of Shear-Wave Splitting Parameters In the Presence of Two Anisotropic Layers. Geophys. J. Int. 119, 949–963.
Tapponnier, P., Zhiqin, X., Roger, F., Meyer, B., Arnaud, N., Wittlinger, G., Jingsui, Y., 2001. Oblique Stepwise Rise and Growth of the Tibet Plateau. Science 294, 1671–1677.
Walker, K.T., Bokelmann, G.H.R., Klemperer, S.L., Bock, G., 2005. Shear-wave splitting around the Eifel hotspot: evidence for a mantle upwelling. Geophys. J. Int. 163, 962–980.
Walsh, E., Arnold, R., Savage, M.K., 2013. Silver and Chan revisited. J. Geophys. Res. Solid Earth 118, 5500–5515.
Wang, C.-Y., Flesch, L.M., Silver, P.G., Chang, L.-J., Chan, W.W., 2008. Evidence for mechanically coupled lithosphere in central Asia and resulting implications. Geology 36, 363–366.
Wang, Q., Niu, F., Gao, Y., Chen, Y., 2016. Crustal structure and deformation beneath the NE margin of the Tibetan plateau constrained by teleseismic receiver function data. Geophys. J. Int. 204, 167–179.
Wessel, P., Smith, W.H.F., Scharroo, R., Luis, J., Wobbe, F., 2013. Generic Mapping Tools: Improved Version Released. Eos Trans. Am. Geophys. Union 94, 409–410.
Windley, B.F., Alexeiev, D., Xiao, W., Kröner, A., Badarch, G., 2007. Tectonic models for accretion of the Central Asian Orogenic Belt. Journal of the Geological Society 164, 31–47.
Wu, C., Xu, T., Badal, J., Wu, Z., Teng, J., 2015. Seismic anisotropy across the Kunlun fault and their implications for northward transforming lithospheric deformation in northeastern Tibet. Tectonophysics 659, 91–101.
Wüstefeld, A., Bokelmann, G., Zaroli, C., Barruol, G., 2008. SplitLab: A shear-wave splitting environment in Matlab. Comput. Geosci. 34, 515–528.
Xie, J., Ritzwoller, M.H., Shen, W., Wang, W., 2017. Crustal anisotropy across eastern Tibet and surroundings modeled as a depth-dependent tilted hexagonally symmetric medium. Geophys. J. Int. 209, 466–491.
Ye, Z., Gao, R., Li, Q., Zhang, H., Shen, X., Liu, X., Gong, C., 2015. Seismic evidence for the North China plate underthrusting beneath northeastern Tibet and its implications for plateau growth. Earth Planet. Sci. Lett. 426, 109–117.
Ye, Z., Li, Q., Gao, R., Zhang, H., Shen, X., Liu, X., Gong, C., 2016. Anisotropic regime across northeastern Tibet and its geodynamic implications. Tectonophysics 671, 1–8.
Yin, A., Harrison, T.M., 2000. Geologic Evolution of the Himalayan-Tibetan Orogen. Annu. Rev. Earth Planet. Sci. 28, 211–280.
Yin, A., Dang, Y.-Q., Zhang, M., Chen, X.-H., McRivette, M.W., 2008. Cenozoic

tectonic evolution of the Qaidam basin and its surrounding regions (Part 3): Structural geology, sedimentation, and regional tectonic reconstructionCenozoic evolution of Qaidam Basin. GSA Bulletin 120, 847–876.

Yuan, D.-Y., Ge, W.-P., Chen, Z.-W., Li, C.-Y., Wang, Z.-C., Zhang, H.-P., Zhang, P.-Z., Zheng, D.-W., Zheng, W.-J., Craddock, W.H., Dayem, K.E., Duvall, A.R., Hough, B.G., Lease, R.O., Champagnac, J.-D., Burbank, D.W., Clark, M.K., Farley, K.A., Garzione, C.N., Kirby, E., Molnar, P., Roe, G.H., 2013. The growth of northeastern Tibet and its relevance to large-scale continental geodynamics: A review of recent studies. Tectonics 32, 2013TC003348.

Zhang, H., Teng, J., Tian, X., Zhang, Z., Gao, R., Liu, J., 2012. Lithospheric thickness and upper-mantle deformation beneath the NE Tibetan Plateau inferred from S receiver functions and SKS splitting measurements. Geophys. J. Int. 191, 1285–1294.

Zhang, P., Burchfiel, B.C., Molnar, P., Zhang, W., Jiao, D., Deng, Q., Wang, Y., Royden, L., Song, F., 1991. Amount and style of Late Cenozoic Deformation in the Liupan Shan Area, Ningxia Autonomous Region, China. Tectonics 10, 1111–1129.

Zhang, P.-Z., Shen, Z., Wang, M., Gan, W., Bürgmann, R., Molnar, P., Wang, Q., Niu, Z., Sun, J., Wu, J., Hanrong, S., Xinzhao, Y., 2004. Continuous deformation of the Tibetan Plateau from global positioning system data. Geology 32, 809–812.

Zheng, D., Zhang, P.-Z., Wan, J., Yuan, D., Li, C., Yin, G., Zhang, G., Wang, Z., Min, W., Chen, J., 2006. Rapid exhumation at ~8 Ma on the Liupan Shan thrust fault from apatite fission-track thermochronology: Implications for growth of the northeastern Tibetan Plateau margin. Earth and Planetary Science Letters 248, 198–208.

Zhao, J., Yuan, X., Liu, H., Kumar, P., Pei, S., Kind, R., Zhang, Z., Teng, J., Ding, L., Gao, X., Xu, Q., Wang, W., 2010. The boundary between the Indian and Asian tectonic plates below Tibet. Proc. Natl. Acad. Sci. 107, 11229–11233.

Zhao, W., Kumar, P., Mechie, J., Kind, R., Meissner, R., Wu, Z., Shi, D., Su, H., Xue, G., Karplus, M., Tilmann, F., 2011. Tibetan plate overriding the Asian plate in central and northern Tibet. Nat. Geosci. 4, 870–873.

Zhu, D.-C., Wang, Q., Zhao, Z.-D., Chung, S.-L., Cawood, P.A., Niu, Y., Liu, S.-A., Wu, F.-Y., Mo, X.-X., 2015. Magmatic record of India-Asia collision. Sci. Rep. 5, 14289.

Zuza, A.V., Cheng, X., Yin, A., 2016. Testing models of Tibetan Plateau formation with Cenozoic shortening estimates across the Qilian Shan–Nan Shan thrust belt. Geosphere 12, 501–532.

Figure captions.

Fig. 1: (a) Tectonics in and around the Tibetan Plateau. Dashed lines denote major

tectonic boundaries. Red arrows denote GPS observations relative to stable Eurasia (Gan et al., 2007). (b) The strain rates inverted from GPS measurements in and around the Tibetan Plateau (Kreemer et al., 2014). Purple lines show the major sinistral faults in the NE Tibetan Plateau, i.e., the Altyn-Tagh Fault (ATF), the Kunlun Fault (KLF), and the Haiyuan Fault (HYF).

Fig. 2: (a) Distribution of 173 stations (blue triangles) used in this study. Yellow lines denote active faults (Deng et al., 2003). Gray lines denote smoothed topography for reference in later figures. Circles and red stars show the earthquakes of magnitudes $M\,4.5-6.0$ and $\geq M6.0$, respectively, occurring from 1920 to 2017 (https://earthquake.usgs.gov). (b) Distribution of 92 events ($\geq M5.5$; blue circles) used in this study. Magenta lines denote major plate boundaries (Bird, 2003).

Fig. 3: Statistics of (a) the dominant periods, (b) backazimuths and their orthogonal directions of null measurements, (c) delay times δt, and (d) fast polarizations φ for the measurements in the high- (HF: 2-8 s; red) and low-frequency bands (LF: 8-20 s; blue). Black arrows in (b) and (d) denote the absolute plate motion (APM) of stable Eurasia in the HS3-NUVEL-1A model (Gripp and Gordon, 2002).

Fig. 4: "Good" (red) and "fair" (blue) splitting parameters measured at 8-20 s (LF). The orientations of the short bars denote the fast polarizations (φ) while the lengths denote the delay times (δt) according to the scale in the bottom-left inset. Gray bars denote SKS splitting measurements in Chang et al. (2017). The large

black arrow denotes the APM direction of stable Eurasia. For the other labeling, see Fig. 2.

Fig. 5: The same as Fig. 4 but for measurement in 2-8 s (HF) band.

Fig. 6: Two-layer splitting measurements. Magenta arrows and circles denote lateral and vertical GPS velocities, respectively, of crustal motions (Gan et al., 2007; Liang et al., 2013), with scale shown in inset. Cyan and orange circles indicate crustal uplift and subsidence relative to ITRF2008, respectively. Blue and red rose diagrams show histograms of lower-layer and upper-layer fast polarizations for the two-layer anisotropy models with $R^* \geq 0.20$ (see the text for details), respectively. (inset) Distribution of the parameters of two-layer anisotropy models. Circles and crosses denote splitting parameters of the lower and upper layers, respectively. Green symbols show the model of Li et al. (2011) for reference. Yellow rose diagrams show the histograms of fast polarizations for HF measurements at 2-8 s (HF) (Fig. 3d). For the other labeling, see Fig. 1.

Fig. 7: Comparison between HF measurements at 2-8 s (orange bars) and the average S-wave velocity in the mid-lower crust based on a published surface wave tomographic model (Bao et al., 2013). Dark gray bars denote the measurements based on Pms phases (Kong et al., 2016; Shen et al., 2015; Wang et al., 2016); note that the scale for delay times of Pms measurements is twice as that of the shear-wave splitting measurements in this study. The dashed line denotes the profile shown in Fig. 8. For the other labeling, see Fig. 2.

Fig. 8: Topography and seismological results along a SW-NE profile extending from the Tibetan Plateau to the North China Craton (profile location in Fig. 7). (a) Topography along the profile. Vertical red lines denote the major faults along the profile. (b) Section of S-wave velocity along the profile from surface waves (Bao et al., 2013). Dashed line denotes the Moho derived from the 4 km/s contour of the surface wave velocity model. (c) Red and blue circles with short bars denote fast polarizations (with 95% confidence regions) of the "good" and "fair" splitting measurements (HF: 2-8 s) within 100 km along the profile, respectively. Yellow and gray histograms show the distributions of the upper- and lower-layer fast polarizations for the valid models ($R^* \geq 0.20$) at two grid nodes along the profile. Note that in the region of two-layer splitting (Tibetan Plateau) the (single-layer) HF measurements are more sensitive to the upper-layer anisotropy. Crosses show P-wave velocity anisotropy at 40 km depth along the profile (Huang et al., 2014). Magenta circles denote GPS observations (Gan et al., 2007). (d) Delay times of "good" (red) and "fair" (blue) HF measurements at 2-8 s. The lengths of the short bars denote the uncertainties of individual measurements.

Fig. 9: A 3-D block model explaining the depth-dependent anisotropy in NE Tibetan Plateau revealed in this study. Ellipses denote the strain field in different layers under different tectonic regions. The subfigure in the top left corner shows alternatives—possibly operating at the same time—for explaining both the uplift and splitting patterns.

Figure 1-9
Click here to download Figure: figs.pdf
Figure 1

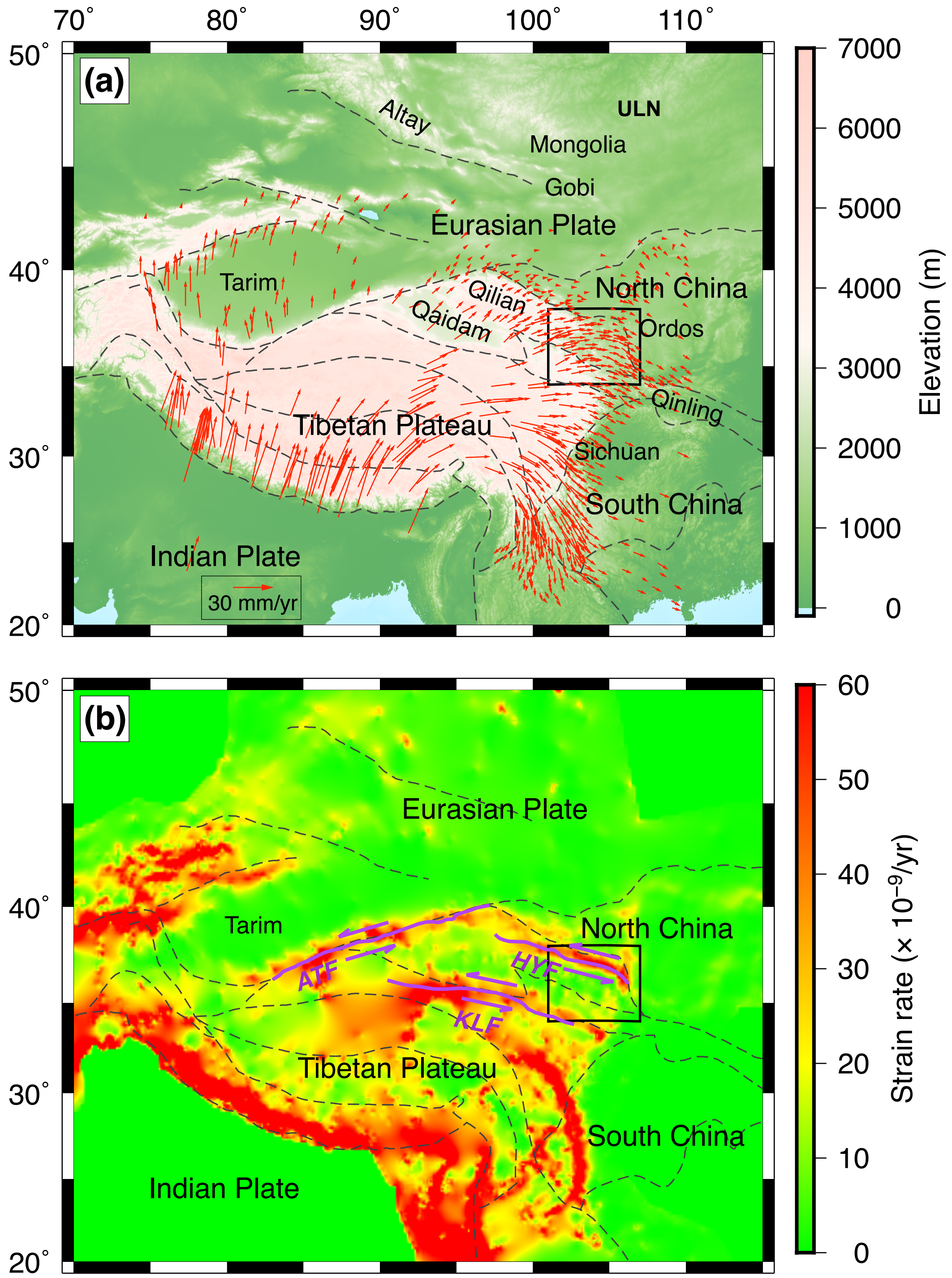

Figure 2

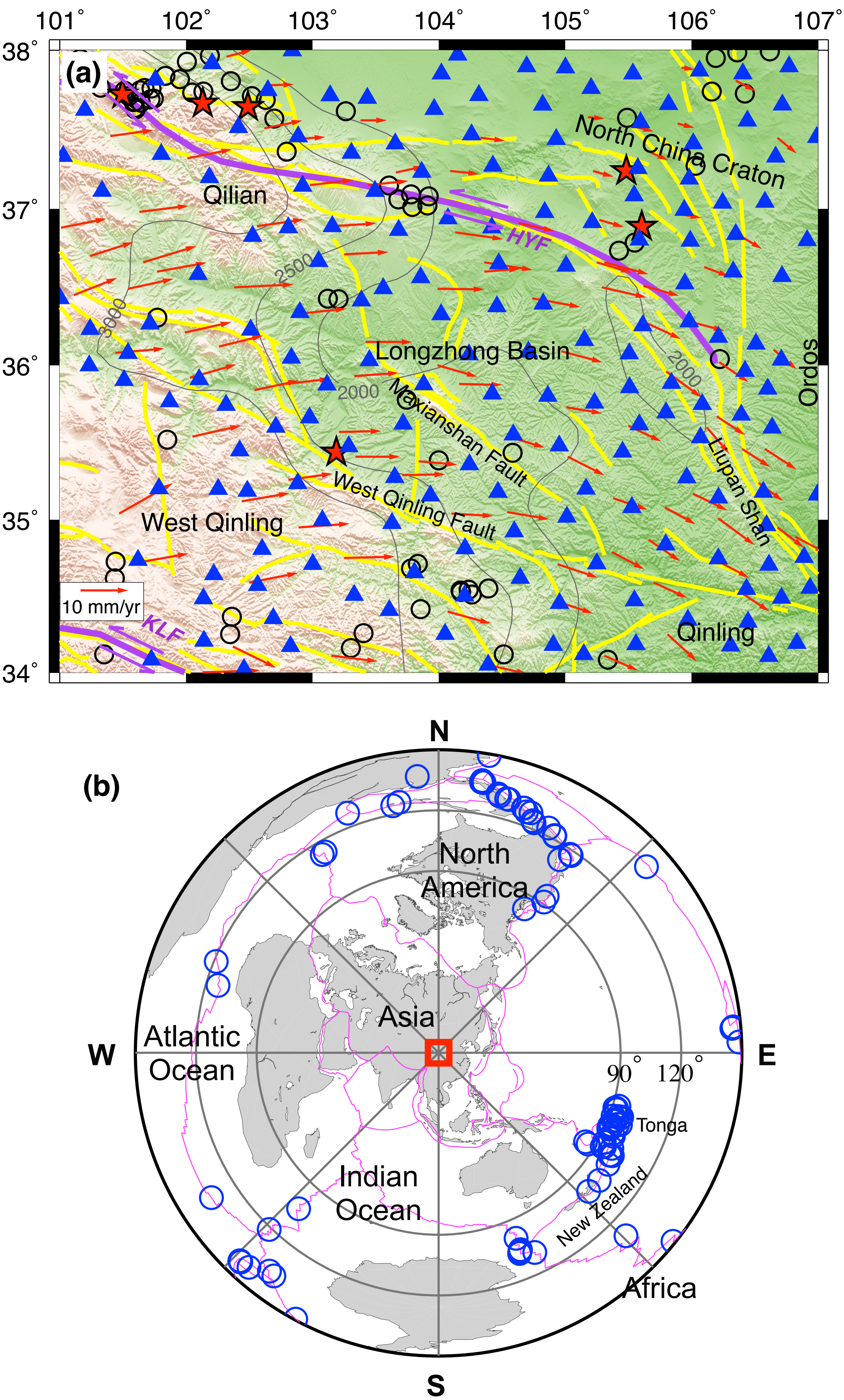

101°
102°
103°
104°
105°
106°
107°
38°
37°
36°
35°
34°
(a)
Qilian
North China Craton
HYF
2500
3000
2000
Longzhong Basin
Maxianshan Fault
Ordos
Liupan Shan
West Qinling Fault
West Qinling
10 mm/yr
KLF
Qinling
N
(b)
North
America
Asia
W
Atlantic
Ocean
E
90°
120°
Tonga
New Zealand
Indian
Ocean
Africa
S

Figure 3

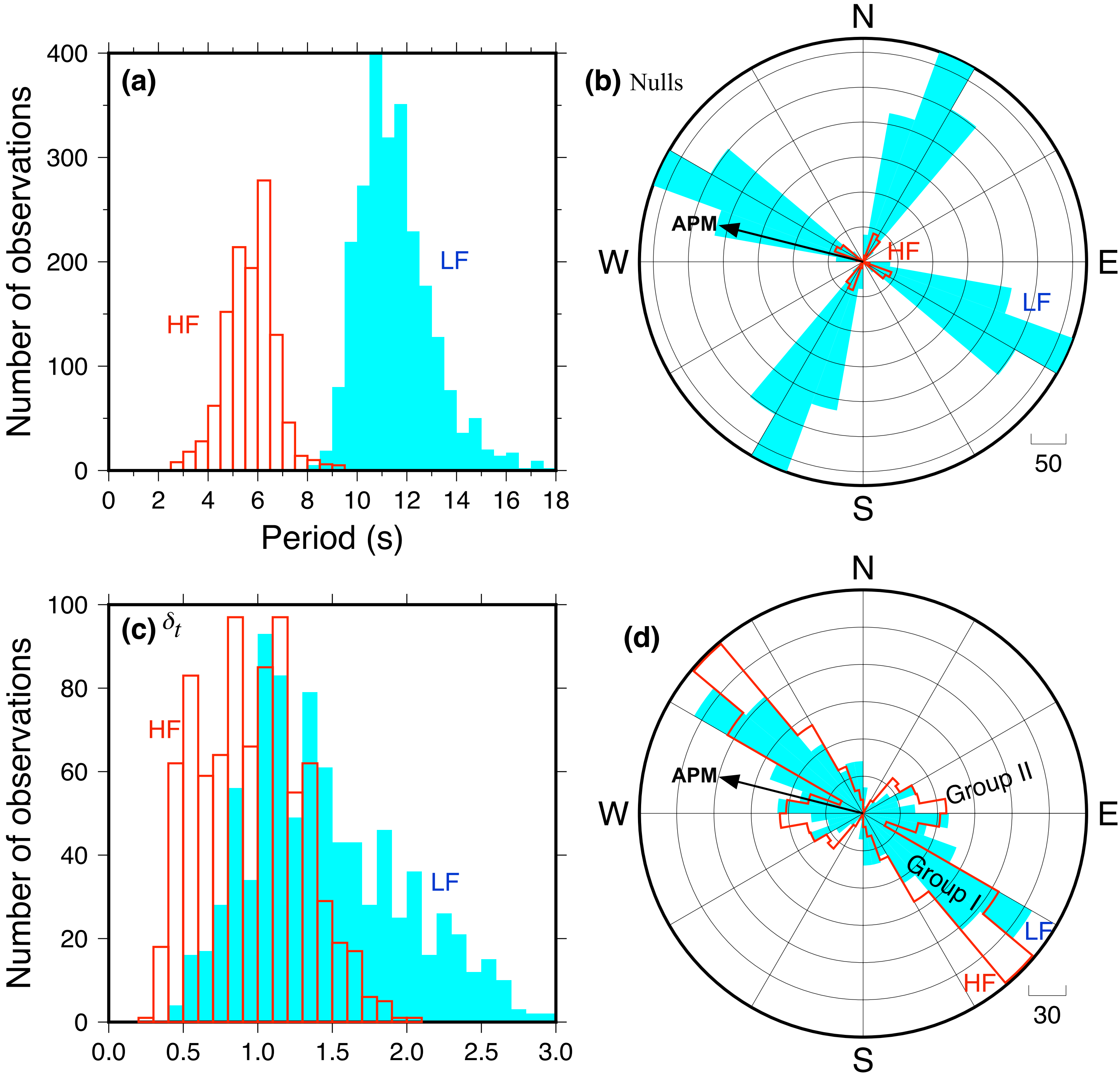

Number of observations
(a)
HF
LF
Period (s)
(b) Nulls
N
S
W
E
APM
HF
LF
50
(c) δ_t
HF
LF
Delay time (s)
(d)
APM
Group II
Group I
LF
HF
30

Figure 4

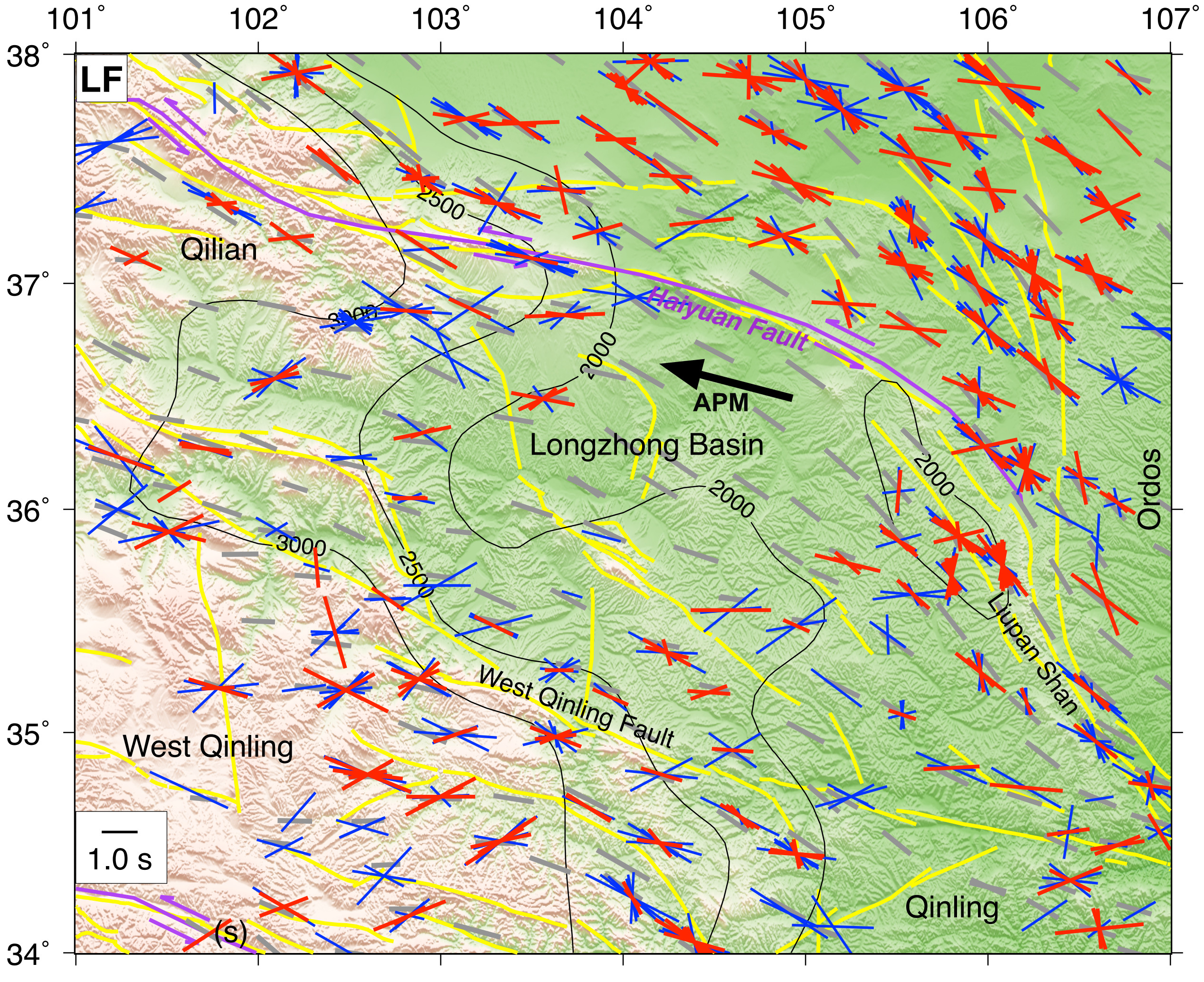

101°
102°
103°
104°
105°
106°
107°
38°
37°
36°
35°
34°
LF
Qilian
Haiyuan Fault
APM
Longzhong Basin
Ordos
Liupan Shan
West Qinling Fault
West Qinling
Qinling
1.0 s
(s)
2500
3000
2000

Figure 5

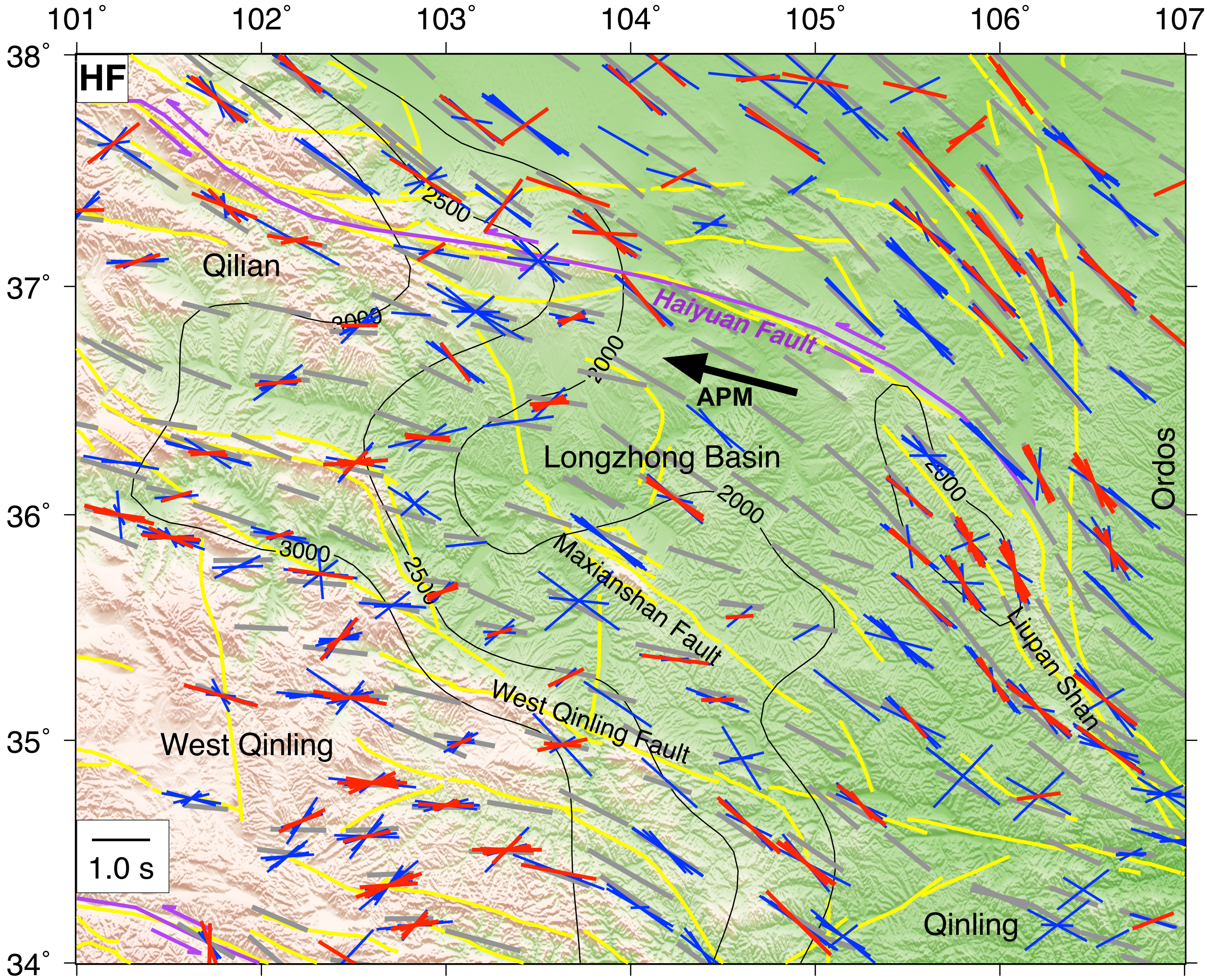

101°
102°
103°
104°
105°
106°
107°
38°
37°
36°
35°
34°
HF
Qilian
Haiyuan Fault
APM
Longzhong Basin
Ordos
Maxianshan Fault
Liupan Shan
West Qinling Fault
West Qinling
Qinling
1.0 s
2500
3000
2000

Figure 6

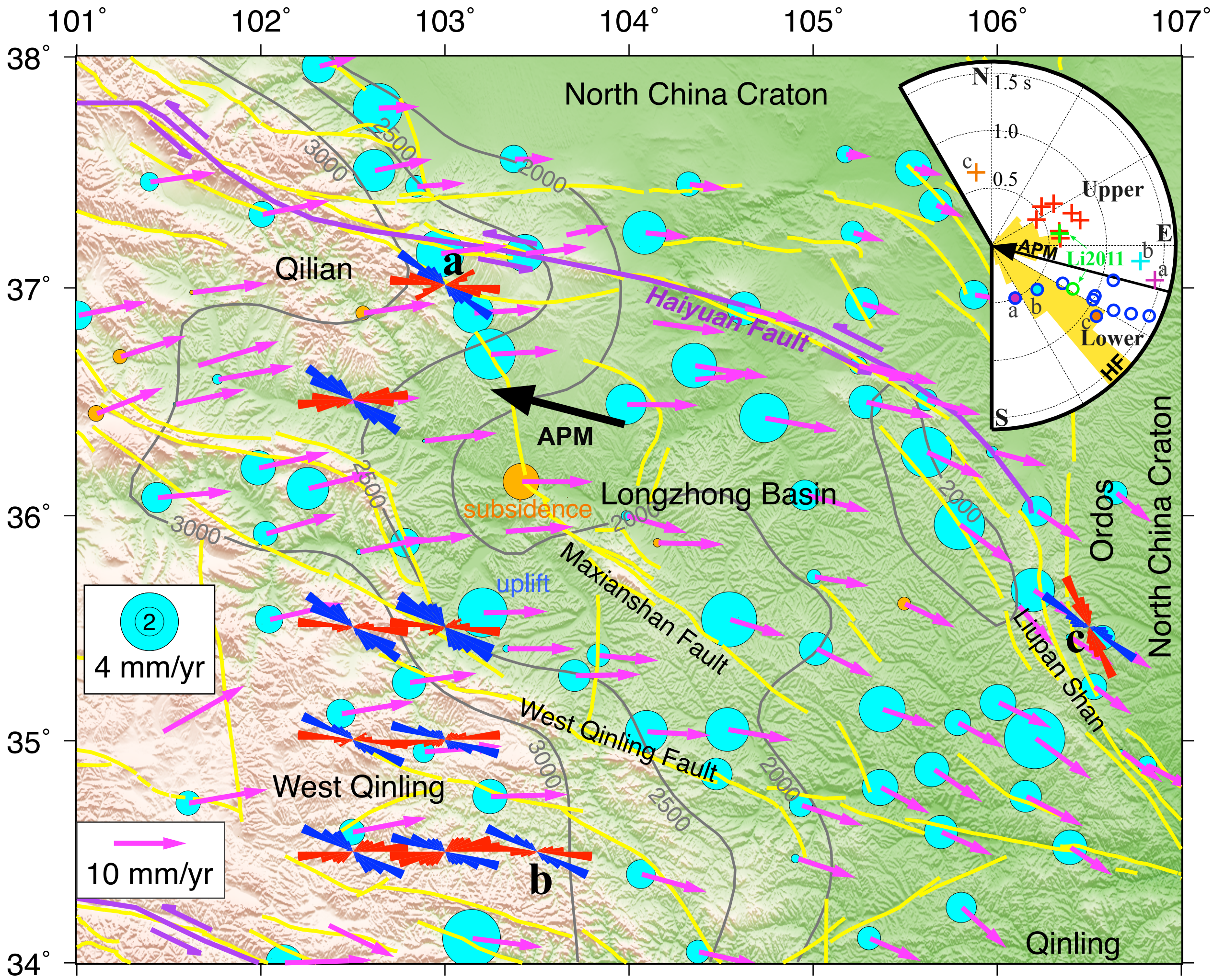

101° 102° 103° 104° 105° 106° 107°
38° 37° 36° 35° 34°
North China Craton
Qilian
Haiyuan Fault
APM
Longzhong Basin
subsidence
uplift
Maxianshan Fault
West Qinling Fault
West Qinling
Liupan Shan
Ordos
North China Craton
Qinling
a
b
c
2
4 mm/yr
10 mm/yr
3000
2500
2000
N
E
S
1.5 s
1.0
0.5
Upper
Lower
Li2011
HF

Figure 7

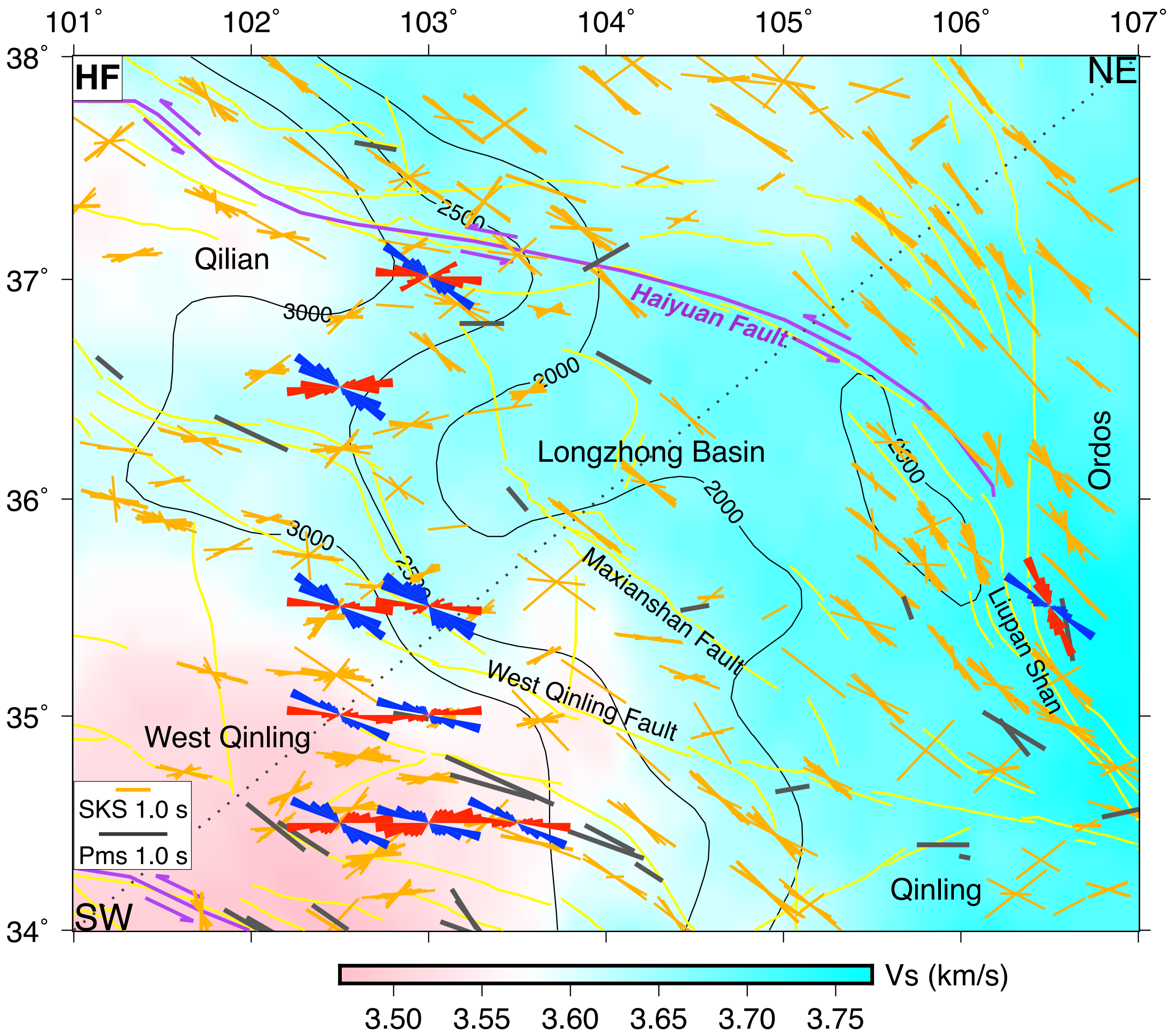
101°
102°
103°
104°
105°
106°
107°
38°
37°
36°
35°
34°
HF
NE
SW
Qilian
Haiyuan Fault
Longzhong Basin
Ordos
Maxianshan Fault
West Qinling Fault
Liupan Shan
West Qinling
Qinling
2500
3000
2000
SKS 1.0 s
Pms 1.0 s
Vs (km/s)
3.50
3.55
3.60
3.65
3.70
3.75

Figure 8

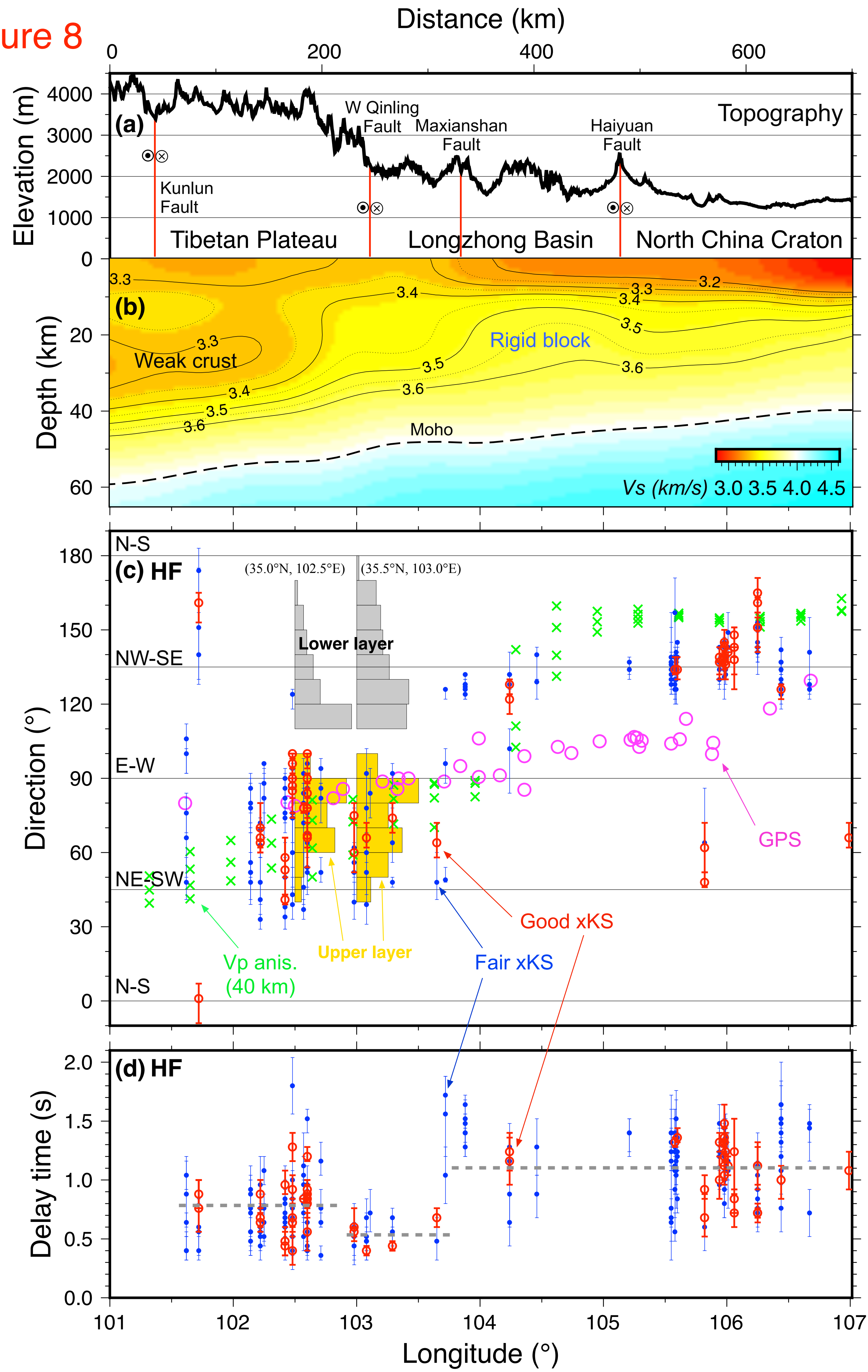

Distance (km)
0
200
400
600
Elevation (m)
4000
3000
2000
1000
0
(a)
Topography
Kunlun Fault
W Qinling Fault
Maxianshan Fault
Haiyuan Fault
Tibetan Plateau
Longzhong Basin
North China Craton
Depth (km)
(b)
Weak crust
Rigid block
Moho
Vs (km/s) 3.0 3.5 4.0 4.5
Direction (°)
(c) HF
N-S
NW-SE
E-W
NE-SW
(35.0°N, 102.5°E)
(35.5°N, 103.0°E)
Lower layer
Upper layer
Vp anis. (40 km)
Fair xKS
Good xKS
GPS
Delay time (s)
(d) HF
Longitude (°)

Figure 9

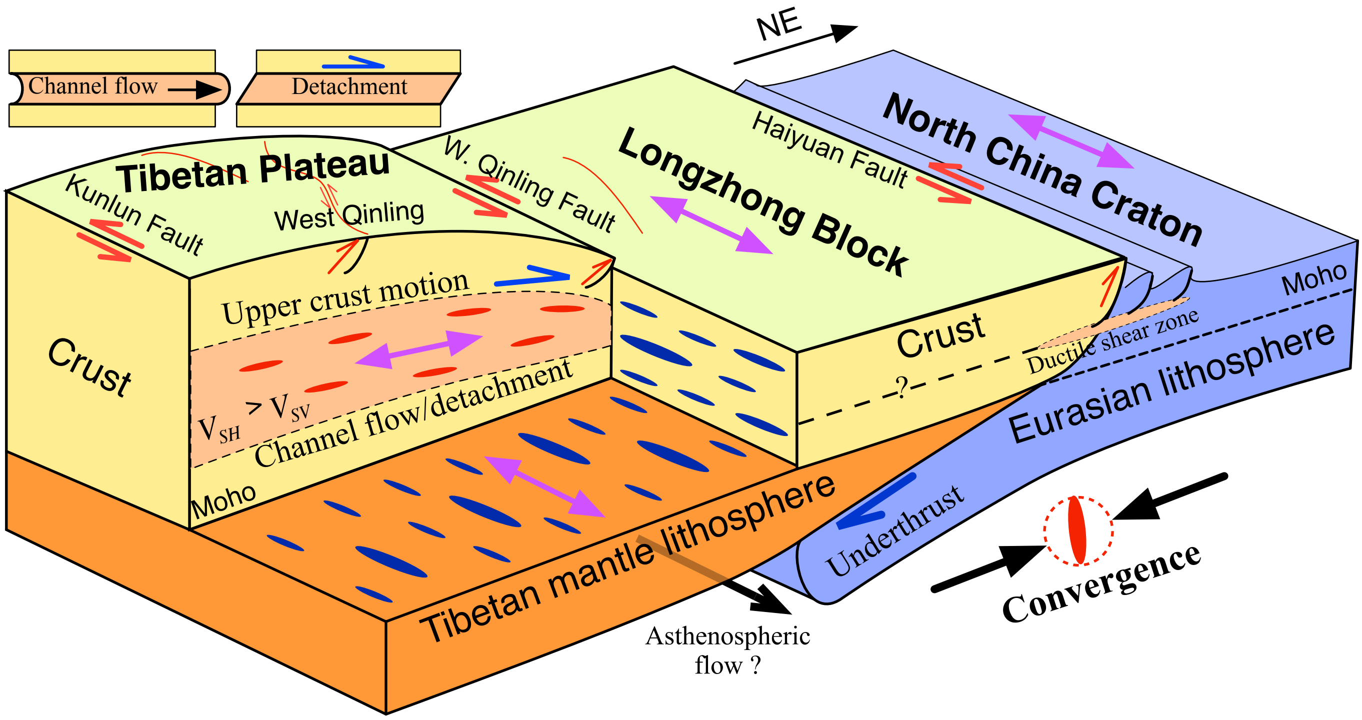

Channel flow
Detachment
NE
Tibetan Plateau
Kunlun Fault
West Qinling
W. Qinling Fault
Longzhong Block
Haiyuan Fault
North China Craton
Crust
Upper crust motion
$V_{SH} > V_{SV}$
Channel flow/detachment
Moho
Crust
?
Ductile shear zone
Moho
Eurasian lithosphere
Tibetan mantle lithosphere
Underthrust
Asthenospheric flow ?
Convergence